




Hybrid in-beam PET- and Compton prompt-gamma imaging aimed at enhanced proton-range verification

J. Balibrea-Correa^{1,a} , J. Lereñdegui-Marco¹, I. Ladarescu¹, C. Guerrero^{2,3}, T. Rodríguez-González^{2,3}, M. C. Jiménez-Ramos^{3,4}, B. Fernández-Martínez^{2,3}, C. Domingo-Pardo¹

¹ Instituto de Física Corpuscular, CSIC-University of Valencia, Valencia, Spain

² University of Seville, 41012 Seville, Spain

³ Centro Nacional de Aceleradores (U. Sevilla, CSIC, Junta de Andalucía), 41092 Sevilla, Spain

⁴ Department of Applied Physics II, ETSA, University of Seville, Seville, Spain

Received: 22 July 2022 / Accepted: 19 October 2022
© The Author(s) 2022

Abstract We report on a hybrid in-beam PET and prompt-gamma Compton imaging system aimed at quasi real-time ion-range verification in proton-therapy treatments. Proof-of-concept experiments were carried out at the radiobiology beam line of the CNA cyclotron facility using a set of two synchronous Compton imagers and different target materials. The time structure of the 18 MeV proton beam was shaped with a series of beam-on and beam-off intervals, thereby mimicking a pulsed proton beam on a long time scale. During beam-on intervals, Compton imaging was performed utilizing the high energy γ -rays promptly emitted from the nuclear reactions occurring in the targets. In the course of the beam-off intervals in situ positron-emission tomography was accomplished with the same imagers using the β^+ decay of activated nuclei. The targets used were stacks of different materials covering also various proton ranges and energies. A systematic study on the performance of these two complementary imaging techniques is reported and the experimental results interpreted on the basis of Monte Carlo calculations. The results demonstrate the possibility to combine both imaging techniques in a concomitant way, where high-efficiency prompt-gamma imaging is complemented with the high spatial accuracy of PET. Empowered by these results we suggest that a pulsed beam with a suitable duty cycle, in conjunction with in situ Compton- and PET-imaging may help to attain complementary information and quasi real-time range monitoring with high accuracy.

1 Introduction

Accurate ion-range determination is a key aspect in modern proton-therapy treatments [1]. This technique allows one to target very precisely the tumor area thanks to the large energy deposition at the end of the proton track (Bragg peak). As a consequence, proton therapy minimizes damage in neighbouring tissues, thereby reducing also long-term secondary effects for such treatments. Hence, it is particularly well-suited for many pediatric cases and tumors close to sensitive organs [1]. However, the full potential of proton therapy is still hindered by the lack of high-accuracy real-time range verification, which would enable to use particle beams as a precise and non-invasive scalpel. This could extend the applicability of proton therapy also to diseases such as ventricular tachycardia and many other cardiovascular disorders [2–4], thereby enlarging the number of patients benefiting from therapeutic high-energy ion beams.

As the incident proton beam slows down and stops inside the patient tissues, nuclear reactions take place all along the projectile path producing quasi-instantaneously (prompt) emission of secondary radiation, mainly γ -rays with energies spanning up to 5–6 MeV [5]. Thus, from the physics point of view, this radiation is especially well suited to monitor the range of the ion beam because of the high spatial and prompt temporal correlation with the primary proton range. On the other hand, from an experimental standpoint, a major challenging aspect for real-time prompt-gamma imaging (PGI) is the small signal-to-background ratio in the clinical environments. The latter is commonly constrained by the low efficiency of the radiation detectors at high γ -ray energies [6–9], by the limited detector performance at high counting rates [1] and by the contaminant radiation arising from proton-beam interactions along different parts of the accelerator gantry [10], which includes also a dominant contribution from neutrons [1, 11–13].

Alternatively, ion-range monitoring via in-beam Positron-Emission Tomography (PET) has been extensively applied in clinical conditions [14–16] and recent experiments with proton- and helium-beams [17–19] have shown very promising results. This methodology is based on the simultaneous detection of two 511 keV annihilation γ -rays coming from the β^+ decay of short-lived ^{12}N nuclei ($t_{1/2}=11$ ms) activated by the hadronic interactions of primary ions. Several configurations have been proposed for

^a e-mail: javier.balibrea@ific.uv.es (corresponding author)

in-beam PET imaging, from systems based on two detection modules working in time-coincidence [17–19] to complex cylindrical ring configurations [20–23]. Some of the challenges of the PET approach are related to the relatively long positron range of ^{12}N (18 mm RMS 1D distance in water [24]), the worsening of resolution along the treatment due to the increasing contribution of longer-lived nuclei [18] and the generally large backgrounds at low γ -ray energies, that lead to very low true statistics for real-time implementation [25, 26].

In 2016 the concept of hybrid detection systems was discussed by Parodi [27], as an alternative to overcome some of the aforementioned limitations. In this new concept, high-energy prompt-gamma imaging is combined with the PET technique. As suggested in Ref. [28], this idea could be implemented by adapting systems based on multiple Compton cameras, originally intended for high-sensitivity three-gamma correlations, which can be exploited for some unstable nuclei, whose β^+ decay is accompanied by an additional de-excitation γ -ray [28]. As discussed in Ref. [27], one could expect that hybrid PGI-PET systems will open new perspectives for in-vivo real-time range monitoring. This statement relies on the complementarity of both techniques, as prompt-gamma emission is, on the one hand, more promising for real-time monitoring, whereas PET imaging can provide tomographic and functional information, interesting to monitor physiological processes and tumour response.

In the present work we report on a detection system, originally proposed for nuclear experiments of astrophysical interest [29], but which enables the simultaneous implementation of the two aforementioned techniques: in-beam PET and Compton PGI. To the best of our knowledge, this work represents the first implementation and demonstration with ion beams of such a hybrid Compton PGI and PET system, as the one proposed in Refs. [27, 28]. The performance of the proposed system for in-beam range monitoring via Compton PGI has been studied in detail in a previous work, on the basis of Monte Carlo simulations [30, 31]. Thus, the objective of the present study was twofold. On the one side, to perform an experimental validation of the Compton-imaging performance envisaged in our previous MC study [30]. On the other hand, to carry out first proof-of-concept measurements to demonstrate the capability of our hybrid imaging system for performing simultaneously PET and PGI with a proton beam. Furthermore, combining two independent techniques for ion-range monitoring, PET and PGI, may provide an enhanced accuracy from the point of view of the systematic and statistical uncertainties. Finally, realizing both techniques with the same apparatus allows one to perform a comparative study, where the advantages and limitations of combining them within the same hybrid system can be addressed in detail. In Ref. [32] we presented already preliminary results of one part of these measurements, which are reported here in more detail and in combination with several other results and conclusions.

The measurements were carried out at the 18 MeV Cyclotron facility of the Centro Nacional de Aceleradores (CNA), Seville [33]. Radiobiological research using this type of low energy particle accelerators has attracted significant interest in the last decades concurring with the worldwide expansion of hadron-therapy centers [34]. Although the proton beam energy used in this work is still between a factor of 5 and 10 lower than the one used in clinical treatments, in combination with the customized set-up described in Sect. 2, it still allowed us to carry out a proof-of-concept demonstration of the simultaneous PET-Compton in-beam imaging. Data-reduction, detector calibration and reconstruction algorithms are discussed in Sect. 3. Section 4 describes the in situ calibration measurements made for validating and characterizing the detector performance, both in terms of PET and Compton γ -ray imaging. The proof-of-concept measurements for the simultaneous PET-Compton imaging are reported in Sect. 5. Finally, Sect. 6 provides a general discussion of the results obtained and future steps.

2 Experimental setup

Our detection system is based on two modular and high efficiency Compton cameras, called i-TED [29], in a front-to-front configuration around the beam-axis (see Fig. 1). Hereafter they are referred to as i-TED-A and i-TED-B. Both i-TED modules can be operated in synchronous mode, thus enabling both PET- and Compton-imaging at the same time, as described below. In order to maximize detection efficiency each i-TED module consists of two planes of Position Sensitive Detectors (PSDs) and each PSD uses the largest commercially available $\text{LaCl}_3(\text{Ce})$ monolithic scintillation crystals. The front PSD or scatter detector has a size of $50 \times 50 \times 15 \text{ mm}^3$, while the rear or absorber detection plane is based on an array of four PSDs, each of them with a size of $50 \times 50 \times 25 \text{ mm}^3$ [35]. Each scintillation crystal is optically coupled to a 8×8 pixels silicon photomultiplier (SensL ArrayJ-60035-65P-PCB). The γ -ray hit 3D-position reconstruction in each PSD is implemented with the methodology described in Ref. [36].

Compton imaging is accomplished by means of γ -ray hit events detected in time coincidence both in the scatter-PSD and any of the four rear PSDs in each i-TED module. For a point-like 1 MeV γ -ray source at 5 cm distance from the front face of the module, the detection efficiency is $\sim 0.2\%$ using time-coincidences between scatter- and absorber-planes of the i-TED module.

For PET imaging time-coincidences of any PSD between i-TED-A and i-TED-B are utilized. This includes coincidences between scatter-scatter, scatter-absorber and absorber-absorber PSDs of i-TED-A and i-TED-B (see also Fig. 6 in Sect. 3).

It is also worth noting that, although the i-TED imagers were specifically designed for nuclear physics experiments using the neutron Time-Of-Flight (TOF) technique [29, 37, 38], from the experimental standpoint there are significant similarities with ion-range monitoring in hadron-therapy, which we have described in detail in our previous work [30–32].

Regarding neutron-induced backgrounds $\text{LaCl}_3(\text{Ce})$ ensures a small sensitivity to neutron interactions in the detection volume itself [30, 31], while preserving also a high intrinsic detection efficiency for γ -rays. Finally, a high time-resolution can be obtained with the implemented acquisition system based on PETsys Front-End Board D version 2 (FEB/D-1024) [39]. Crystal-delay and

Fig. 1 Picture of the setup used in the proof-of-concept experiment at CNA. The proton-beam (red arrow) impinges from the left-hand side and punches through five thin plastic foils surrounded by two i-TED modules in front-to-front configuration

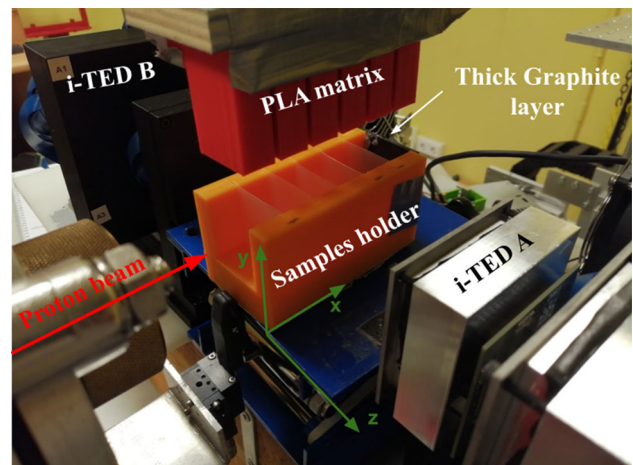
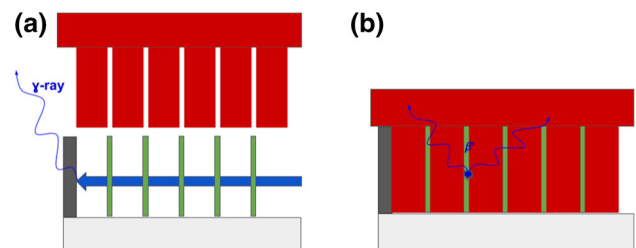


Fig. 2 Schematic drawing of the experimental setup during the different parts of the duty cycles. The thin layers under study are represented by green color, the thick graphite layer by gray and the PLA matrix by red color, respectively. Panel a shows the experimental setup during the beam-on period. In panel b is displayed the experimental setup during the beam-off period



time-walk effect calibrations can lead to coincidence-time resolutions (CTRs) of several 100 ps [40], which in turn can help to reduce random coincidences and other related backgrounds. At this stage, no such corrections were implemented in our system yet, leading to a CTR of about 1 ns FWHM at 511 keV γ -ray energy. For further details on the i-TED modules and developments the reader is referred to Refs. [35, 36, 41] and references therein.

The cyclotron facility at CNA used for the present proof-of-concept experiment consists of a Cyclone 18/9 model equipped with an external beam line for multi-purpose research. The cyclotron accelerates protons and deuterons to 18 and 9 MeV, respectively. The beam is then delivered to the dedicated experimental area through a complex beam extraction system. For further details about the research beam line the reader is referred to Ref. [42].

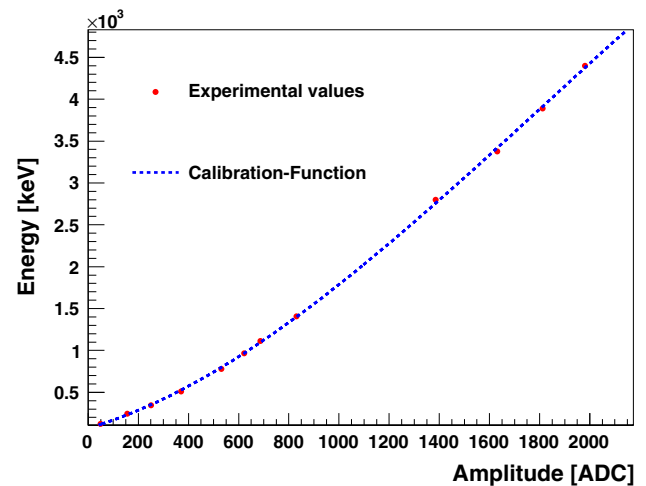
During the experiment, a proton beam with an energy of 18 MeV was delivered to the experimental area with current values varying from 500 pA up to 1 nA on target, adding-up a total charge ranging from 212 to 674 nC per irradiation, depending on the total irradiation time and specific duty cycle, which will be explained later.

A picture of the experimental setup is displayed in Fig. 1. Apart from the PET-Compton imaging objective described in this article, this specific configuration was chosen also with the aim of measuring proton-induced β^+ -emitter production cross sections, following a similar methodology as the one reported in the previous works [43, 44]. The proton beam direction is indicated in Fig. 1 by the red arrow. A sample holder (elongated U-shaped piece in the center) was used to simultaneously expose regularly spaced sample-foils to the proton beam. The holder was aligned with the proton beam axis, thereby inducing a similar irradiation field for all samples under study. The material of the sample holder was polylactic acid (PLA) plastic with a size of $5.2 \times 5.5 \times 10.3 \text{ cm}^3$. The central hole had a size of $3.2 \times 4.12 \text{ cm}^2$. The samples consisted of thin layers of different materials, described below, which were placed in five dedicated slots with a regular gap of 16 mm. The samples had a square size of $41.2 \times 41.2 \text{ mm}^2$ and a thickness of 0.8 mm. Two different materials were used, Nylon and PMMA, with nominal densities of 1.15 and 1.18 g/cm^3 , respectively. At the very end of the samples holder a 2-mm-thick graphite layer was added, with the twofold purpose of fully stopping the proton beam and registering the proton-current values during the experiment.

The sample-holder was supplemented with a movable PLA matrix, also shown in Fig. 1. This PLA matrix was remotely inserted and removed. After each proton irradiation the matrix was inserted, thus filling the gap between the samples, acting as β^+ converter and shortening the range of the e^+ particles. Figure 2 shows a schematic drawing of the measurements during proton irradiation (a) and after proton irradiation (b). The measurements made with different materials and beam conditions are described below in Sect. 5.

The two i-TED modules used during the experiment were placed front-to-front on both sides of the proton beam axis, in such a way that the samples under study could be fully covered by the PET field of view of both i-TED imagers. In Fig. 1 the i-TED-A module had an aluminum housing and was placed at 5.9 cm from the sample holder. The second one, i-TED-B, had a black PLA encapsulation and was placed at 5.1 cm from the sample holder. The distance between the front face of the scatter plane of both

Fig. 3 Energy calibration for an individual detector of i-TED-A. The experimental data from the ^{152}Eu calibration source and γ -ray lines PG identified during beam-on periods are represented by the red dot points. The fitted third degree polynomial is plotted by the dashed blue line



i-TED modules was 17.5 cm. The separation between detection planes in each i-TED was set to only 2.6 cm, thereby favoring coincidence efficiency versus angular resolution [35].

The 10 PSDs embedded in both i-TED modules comprised a total of 640 readout channels, which were synchronously acquired by means of two PETsys Front-End Board D version 2 (FEB/D-1024) modules, synchronized by means of a clock & trigger module that used LVDS signals at 400 Mbit/s [39]. The data-stream was read with a Gigabit ethernet connection via the PCI-express board in the acquisition computer for its posterior analysis with the dedicated reconstruction software described in Sect. 3. The performance of the i-TED detectors for both Compton and PET imaging is described below in Sect. 4.

3 Data reduction and algorithms

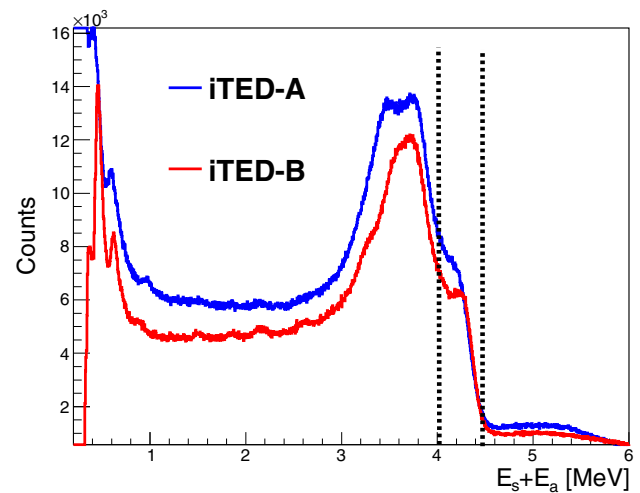
The individual detectors of each i-TED module were calibrated in energy using a point-like ^{152}Eu γ -ray source. In addition, the γ -ray lines corresponding to the strongest nuclear reactions identified during the proton irradiations were included in the energy calibration. The latter correspond to the $^{12}\text{C}(p,p'\gamma)^{12}\text{C}$ and $^{16}\text{O}(p,x\gamma)^{12}\text{C}$ nuclear reactions, both emitting 4.4 MeV γ -quanta [13]. The corresponding first and second escape peaks were also clearly visible and included in the calibration, as well as the 511 keV γ -ray from the detection of β^+ annihilation events during the beam-on periods. A third-order polynomial was used to model the energy-ADC relation over this large deposited energy range. An example of the individual PSD energy calibration is displayed in Fig. 3. The experimental ADC values for the different γ -ray transitions are represented by red markers, while the fitted polynomial is displayed by the dashed-blue line.

The energy detection thresholds obtained for i-TED-A and i-TED-B were of 100 keV to 250 keV for scatters and absorber detection planes, respectively. The γ -ray interaction positions in the individual PSDs were reconstructed following the procedure described in Ref. [36]. The absolute γ -ray position interaction was obtained from the reconstructed intrinsic 3D position coordinates and the location of each PSD, which was well known by set-up construction.

Once the individual $\text{LaCl}_3(\text{Ce})$ detectors have been calibrated in energy, time-coincidence events between different PSD pairs are built, both for PSDs within the same i-TED module (for Compton imaging) or between PSD pairs of different i-TED modules (for PET imaging). The sum-energy value of γ -ray hits in time coincidence is referred to as add-back energy, regardless of the nature of the time-coincidence event: PET, Compton, or random event. As an example, the i-TED add-back spectra during the beam-on period of configuration (I), which is explained in the next section, are displayed in Fig. 4. The time-coincidence window between different detection planes was set to 10 ns, which allowed to reduce random coincidences from other background sources. The deposited energy spectra registered during the different configurations described later in Sect. 5 were similar. This result may indicate that the spectra are dominated by the inelastic reactions in carbon nuclei of the thick graphite layer, an effect which is expected from the Bragg curve [2, 5] and the large amount of material in the thick graphite target when compared to the thin samples of Nylon and PMMA.

The energy window of 4.0-to -4.6 MeV was chosen for the beam-on periods in order to perform Compton imaging (see high energy dashed lines in Fig. 4). A high energy threshold for the individual absorber PSD detectors, 700 keV, was used for the Compton imaging reconstruction aiming to reduce artifacts in the images due to time-correlated pair production events and random coincidences with 511 keV. The image plane chosen for the Compton reconstruction corresponds to the axial direction of the samples holder, i. e. 8.5 cm from the frontal face of the i-TED-A module. Finally, the Compton images in this work were obtained by implementing the analytical inversion algorithm based on spherical harmonics published by Tomotani and Hisarawa in 2002

Fig. 4 Add-back deposited energy spectrum of i-TED-A (blue) and i-TED-B (red) during the beam-on period. The dashed lines indicate the energy-selection around the 4.4 MeV γ -ray line used for Compton imaging



[45]. This inversion formula, which is based on an infinite Legendre polynomial expansion, leads to an approximate solution given by a unit vector in the image space, \mathbf{s} . The image at that vector position is described by

$$f(\mathbf{s}) \approx \int_{\cos \omega_{\min}}^{\cos \omega_{\max}} d \cos \omega \int_S dk^{-1}(\mathbf{t}, \mathbf{p}; \cos \omega) g(\mathbf{t}; \cos \omega), \tag{1}$$

where \mathbf{t} is a unit vector into the projection space, ω_{\min} and ω_{\max} are the minimum and maximum Compton scattering angles that can be measured experimentally with the configuration used for the i-TED modules, $g(\mathbf{t}; \cos \omega)$ is the projection data in the image space and $k^{-1}(\mathbf{t}, \mathbf{p}; \cos(\omega))$ is the inversion kernel. This kernel is defined as

$$k^{-1}(\mathbf{t}, \mathbf{p}; \omega) = \sum_{n=0}^{N_{\max}} \frac{2n + 1}{4\pi H_n} P_n(\cos \omega) P_n(\mathbf{s} \cdot \mathbf{t}) \tag{2}$$

with H_n given by the formula

$$H_n = \int_{\cos \omega_{\min}}^{\cos \omega_{\max}} \sigma(\cos \omega) P_n^2(\cos \omega) d \cos \omega. \tag{3}$$

In the latter expression P_n is the Legendre polynomial of order n and $\sigma(\cos \omega)$ is the Klein–Nishina Compton differential cross-section [46]. N_{\max} is the maximum number of terms involved in the polynomial expansion and it must be chosen according to the angular resolution of the experimental apparatus, i.e., the experimental angular resolution of the i-TED modules that depends on the selected deposited energy window and the distance between detection planes.

The complexity of this algorithm leads to a large computational cost in order to reconstruct a Compton image with sufficient resolution. For this reason, the algorithm was implemented in this work for GPU devices using the CUDA 11.1 toolkit [47]. This methodology allows for a speed-up factor of about ~ 121 , when compared to the singled-threaded CPU version [30]. Additionally, and aiming at quasi-real time image reconstruction in clinical studies, H_n was pre-computed for a wide range of γ -ray energies and Compton scattering angles corresponding to the detectable angular range between ω_{\min} and ω_{\max} . The H_n values were saved in a table format for its posterior use, thus enhancing further the speed of the image reconstruction.

The add-back energy-calibrated spectrum of the i-TED modules during the beam-off period is displayed in Fig. 5. The total add-back spectrum is displayed in blue, while the selected window for the β^+ full-energy coincidence peak used for PET imaging is shown by the red region. This spectrum was obtained using also a time-coincidence window of 10 ns between the individual detectors of different i-TED modules.

The PET images were reconstructed using a simple analytical algorithm, where straight lines of response (LOR) between the γ -ray interaction 3D-positions at each i-TED detector were intersected with the central axial plane. The latter PET imaging plane coincides with the one used for Compton imaging during the beam-on periods, which was at 85 mm from the front face of the i-TED-A module.

A detailed geometry of the experimental setup was implemented in a C++ Monte Carlo (MC) application based on the Geant4 toolkit, version 4.10.6 [48]. The MC simulation included the standard electromagnetic package option 3, the radioactive decay, and the packages commonly used in hadron-therapy simulations [49]. These calculations were helpful for the reliable interpretation of the experimental results, as described later in Sects. 5 and 6. The geometry implemented in the MC code is displayed in Fig. 6. For Compton imaging it includes the two i-TED modules, the sample holder with the samples and the thick graphite layer. For PET imaging the geometry includes also the PLA converter matrix, not shown in Fig. 6. In the simulations, the intrinsic resolutions for both position- and energy-response were included according to the laboratory characterization described in the references [36, 41].

Fig. 5 Add-back deposited time-coincidence energy spectrum of the i-TED modules during the beam-off period. The selected deposited energy window for PET imaging is displayed by the shadowed red region

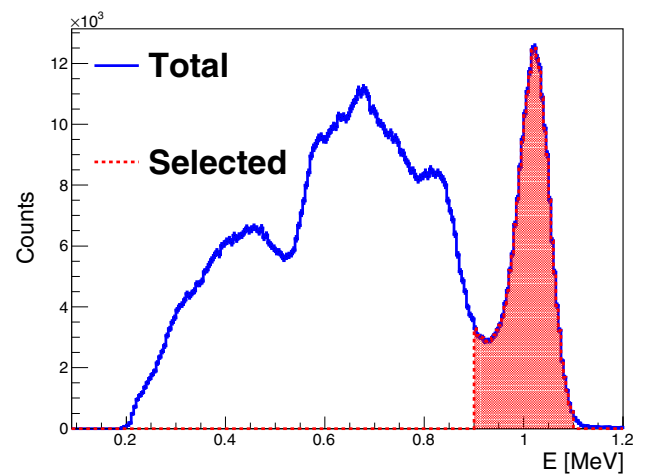


Fig. 6 Geometry of the experimental setup as implemented in the MC simulation. See text for details

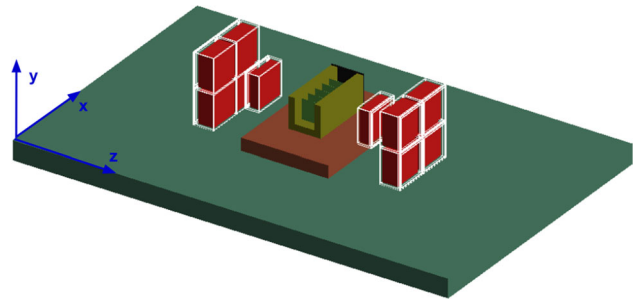
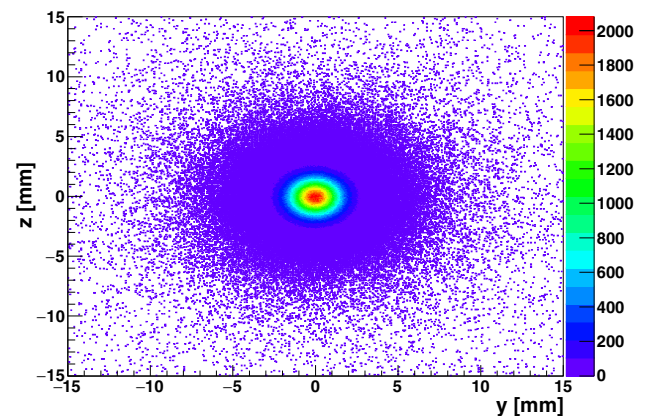


Fig. 7 MC simulation of the proton-beam profile registered in a thick graphite layer



The energy dependence of the energy resolution for the PSD, $R(E)$, was determined from the energy calibration procedure using a functional of the form

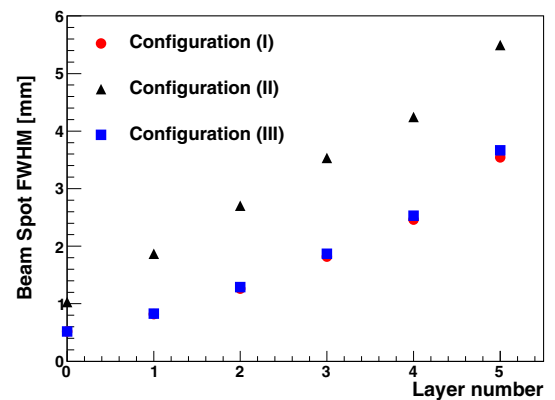
$$R(E) = \sqrt{a + b/E}, \quad (4)$$

where the a and b parameters were adjusted from the experimental energy calibrations. In order to perform a realistic comparison, the MC-calculated Compton- and PET-images were reconstructed by implementing the same algorithms and conditions applied to the experimental data.

A final consideration is required regarding the effect of the proton-beam divergence. As protons interact with the sample material along the beam path a spreading is introduced in the transversal spatial profile of the beam. Because the Compton- and PET-imaging algorithms used in this work are based on a single 2D image plane for the reconstruction, the images obtained will reflect also the broadening due to beam straggling effects. In order to account for this experimental effect a dedicated simulation of the proton beam passing through the stack of samples was performed for the three different configurations described later in Sect. 5. This calculation included the different materials and positions in the experimental setup, as shown in Fig. 6. For each simulation the 3D vertex locations of the inelastic proton scatterings at the different irradiated layers were registered.

As an example, Fig. 7 shows the proton-beam profile calculated at the graphite layer in the first configuration discussed later in Sect. 5. These distributions will be used afterwards as initial emission-vertex distributions for the subsequent MC simulation of the

Fig. 8 MC-calculated FWHM values for the proton beam spatial distribution at the different layers and for the different configurations



prompt γ -rays and e^+ particles in the beam-on and beam-off modes, respectively. The aim for this calculation is twofold. On the one hand, to speed-up the simulation process and get reliable results in a reasonable time and, on the other hand, to estimate the number of expected inelastic interactions for the individual layers, aiming at a better interpretation of the comparison between experimental and Monte Carlo results.

As expected, the full-width-at-half-maximum (FWHM) values of the proton–beam distributions at the different layers increase along the beam direction, as shown in Fig. 8. The main difference between the different configurations (see Sect. 5) was obtained for the configuration (II), where a thick 0.8 mm Nylon-based degrader was placed just before the sample holder to reach lower incident proton energies.

Finally, for the proper interpretation of the results shown later in Sect. 5 it is worth to indicate that for both, PET and Compton, the image reconstruction is made from the reference system of i-TED-B. Thus, the direction of the proton beam in the reconstructed images is from right-to-left, the left-hand side being the position of the thick graphite layer (charge integrator) and the right-hand side the entrance of the proton beam, as it is schematically shown in panel (a) of Fig. 2.

4 In situ characterization of the Compton-PET imaging system

In this section we report on the performance of the two i-TED modules for Compton and PET imaging by comparing MC simulations with data acquired using point-like radioactive sources and well-controlled proton irradiations during the proof-of-concept experiment. The goal of this work is to validate the implemented image-reconstruction algorithms and characterize the systematic behaviour of our detection set-up, as a preceding step to the in-beam Compton-PET imaging application described later in Sect. 5.

4.1 PET imaging

The PET performance was experimentally characterized by using a standard point-like ^{22}Na calibration source placed at the sample-holder slot positions number two, three and four. These positions match with the central region of the imaging system and cover the entire PET field of view between the scatter planes of both i-TED modules. The ^{22}Na sample was placed at the axial-beam distance, thereby matching well the Compton and PET reconstruction planes.

Projections obtained from the PET distributions along the x - (red) and y -axis (blue) for the different source positions are displayed in Fig. 9. These results were obtained using the simple analytical algorithm described in the previous section. In general, the experimental results are in agreement with the MC simulation, which is shown with a black-dashed line.

For this comparison, the MC simulations were scaled to match the height of the experimental distributions. The satisfactory agreement found for peripheral source positions (panels a and c in Fig. 9) indicates that pin-cushion effects in the large monolithic crystals are reasonably well treated by means of the implemented SVM-method described in Ref. [36]. The good agreement for both x - and y -axis projections of the central source position (panel b in Fig. 9), serves to validate also the intrinsic 3D position resolution obtained in our previous work [36] and implemented here in the MC-model.

The PET image resolution displayed in Table 1 for both axes has been determined from the FWHM of a Gaussian fit to the experimental data. As expected, the best resolution in the x -axis is obtained for the central source location (position number three). As one moves away from this point, slightly broader FWHM values are obtained (positions 2 and 4) reflecting a degradation of the PET resolution. This effect can be ascribed to the intrinsic resolution spatial profile of the PSDs, which becomes worse for the peripheral region of the monolithic crystals [36].

The spatial resolution for PET shows an average value of 6.4 (6) mm FWHM. This resolution is in agreement with the one determined by means of MC simulations using individual crystal position reconstructions reported in a previous work [36], and in line with similar pre-clinical PET-imaging prototypes (5–6 mm) as reported, for example, in Ref. [50] and references therein.

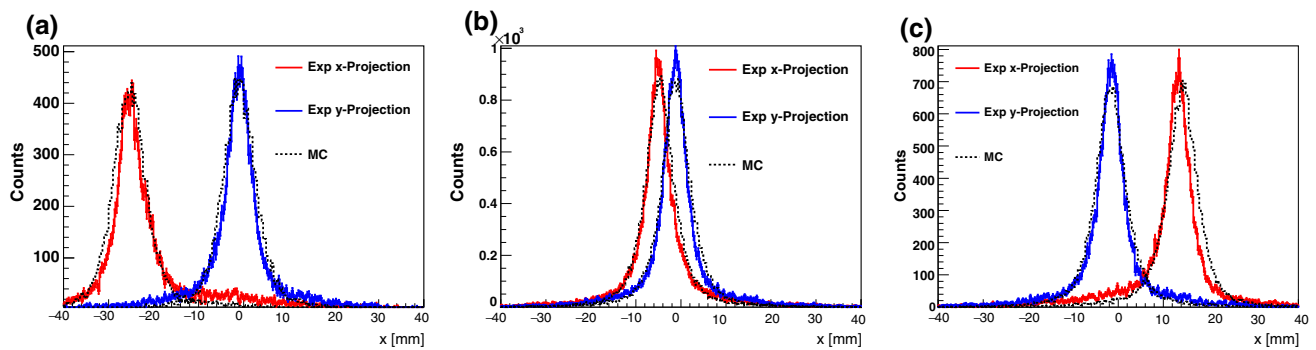


Fig. 9 x - (red) and y -axis (blue) projections of the PET images for the ^{22}Na calibration source at different positions along the sample holder. The result of the MC simulation is shown by the dashed-black curve. Panels a–c correspond to slots number four, three and two in the sample holder (see also Sect. 5)

Table 1 Experimental x - and y -axis FWHM calculated from the experimental ^{22}Na PET image at the different sample positions

Position	FWHM x [mm]	FWHM y [mm]
2	6.1 (1)	6.2 (1)
3	5.6 (1)	6.1 (1)
4	7.4 (1)	6.9 (1)

4.2 Compton imaging

The 2D Compton imaging reconstruction capability and resolution for both i-TED modules at high γ -ray energy was verified by means of a short dedicated measurement with proton beam, where a 1.8-mm-thick graphite layer was placed in the third position of the sample holder, close to the geometrical center of the experimental setup. The incident beam energy was 18 MeV. The 2D images reconstructed with the analytical Compton algorithm described in the previous section are displayed in Fig. 10. For comparison purposes, the figure also shows a point-like 4.4 MeV source simulated at the same position. Differences between experimental and calculated distributions can be ascribed, to some extent, to the spatial profile of the proton beam, of about 2 mm FWHM (Fig. 8), not included here in the simulation.

A small systematic shift in the x -position was identified after a detailed comparison between the images reconstructed in panels (a) and (b) of Fig. 10. Indeed, the position of the graphite layer is reconstructed with a difference of 10(1) mm between i-TED-A and i-TED-B modules along the x -axis. Since the distance between the detectors was well under control, this shift rather indicates that the central axis of both i-TED modules were not perfectly orthogonal to the beam direction (z -axis). According to the differences in the reconstructed positions and the distance between the frontal faces of the i-TED modules a deviation of about 2–3° with respect to the nominal 90° orientation has been estimated. No attempt has been made to correct for such systematic bias because it does not compromise the imaging results and conclusions of the present work. On the other hand, a more precise and reliable mechanical structure is in preparation for future similar measurements.

The FWHM values obtained for both x - and y -axis projections of the reconstructed Compton images (Fig. 10) are reported in Table 2. As expected, the experimental resolutions obtained for both i-TED modules are rather comparable. On the other hand, a difference of ~5–6 mm is found between simulation and experiment. This is most probably to be ascribed to the combination of point-like simulation and the worsening of the intrinsic spatial resolution with increasing γ -ray energy [6], an effect which was not included in the simulation.

5 Proof-of-concept for hybrid Compton-PET measurements

The proof-of-concept measurements with the proton beam were performed in cycles separated in well-defined beam-on and beam-off periods. It is worth to emphasize that the different duty-cycles of the proton beam and the two sample materials were chosen in order to determine production cross-sections of some specific β^+ emitters at different proton-beam energies [43, 44]. For the present work this variety of materials and beam-conditions enabled a systematic study of both Compton- and PET-techniques in terms of accuracy, sensitivity and repeatability.

During beam-on the β^+ converter matrix was placed off-beam, as schematically shown in Fig. 2a, thereby avoiding any interference of the matrix with the incoming proton beam. At this stage all samples under study were irradiated by the proton particles at the same time and in similar amounts. Because of the proton-beam energy loss at each sample, different proton energy ranges were covered at each slot position along the sample holder. The beam was fully stopped in the last layer, a 1.8-mm-thick graphite foil, as shown in Fig. 2.

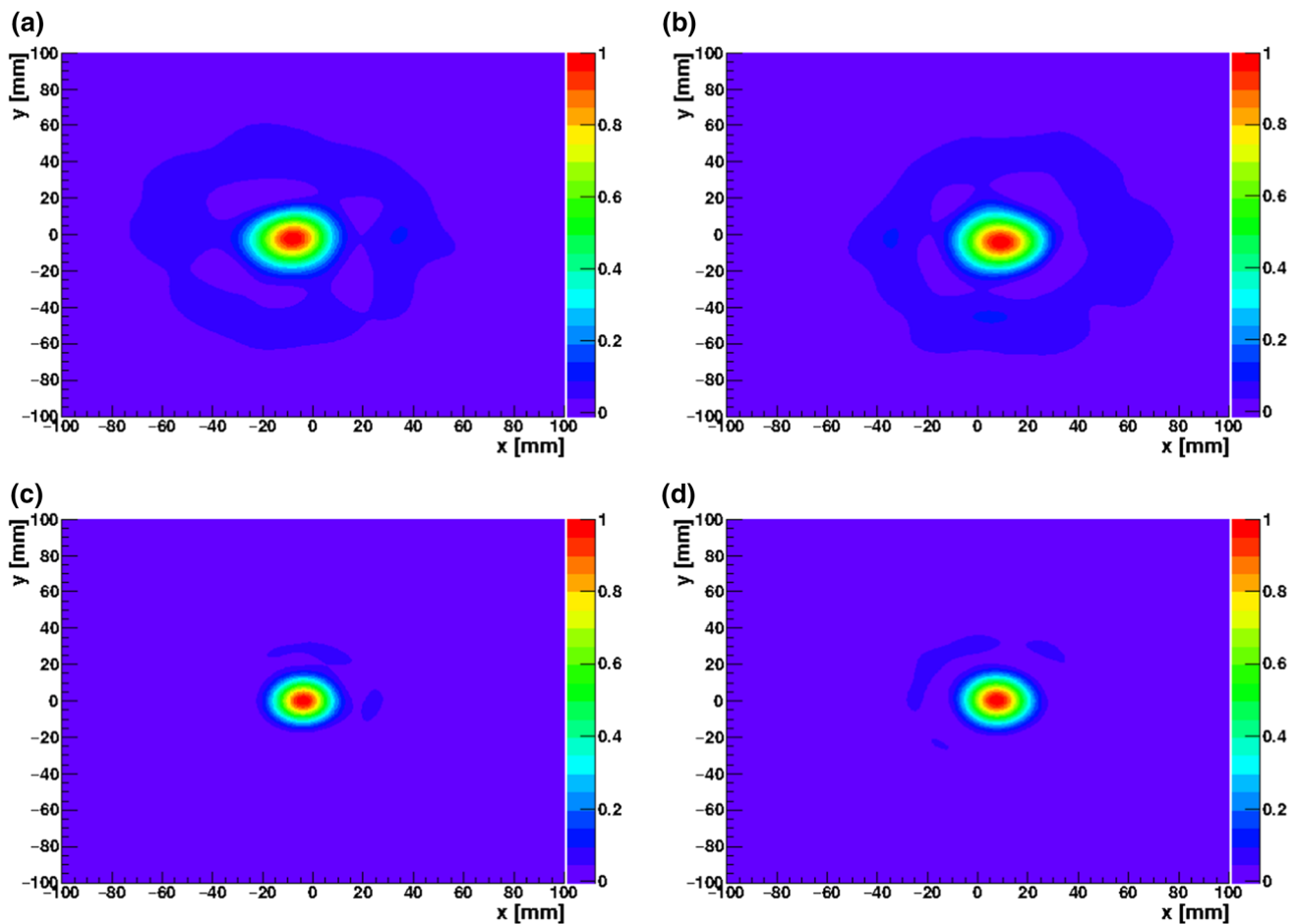


Fig. 10 Compton images using the 4.4 MeV γ -ray transition from experimental data (top panels **a** and **b**) and Monte Carlo simulations (bottom panels **c** and **d**) for the thick graphite layer placed at the third slot position of the sample holder irradiated with the proton beam at CNA. See text for details

Table 2 Experimental and Monte Carlo FWHM calculated from the Compton images reconstructed using the thick graphite layer in the third position of the samples holder

Detector	FWHM x [mm]	FWHM y [mm]
i-TED-A	24.73 (5)	25.12 (3)
i-TED-A (MC)	18.3	18.0
i-TED-B	24.26 (6)	24.73 (4)
i-TED-B (MC)	19.6	19.4

In the beam-on intervals PG Compton imaging is exploited by means of both i-TED modules, which could provide independent spatial information from the high-energy prompt gamma-rays emitted. In the beam-off periods the PLA matrix was swiftly inserted using a remote mechanical actuator, as shown in Fig. 2b. The converter matrix allowed to shorten the mean free-path of the e^+ particles significantly, thus enabling also a precise PET imaging.

Three different sample configurations and duty cycles were used. For sake of clarity, in the following sections we refer to those configurations as the following:

- Configuration (I): Five Nylon layers and one thick graphite beam stopper at the end.
- Configuration (II) Five Nylon layers and, a 0.8-mm-thick Nylon-based proton–beam energy degrader just before the Nylon samples and one thick graphite beam stopper at the end.
- Configuration (III) Five PMMA layers and one thick graphite beam stopper at the end.

The time structure of beam-on and beam-off periods for each individual configuration is graphically represented in Fig. 11. In configuration (I) there were four beam-on irradiations of 240 s duration, each of them followed by 480 s of beam-off (blue-solid line in Fig. 11). Configuration (II) consisted in one long irradiation of 360 s followed by a long beam-off (red-dashed line). Configuration (III) consisted of 2 beam-on periods of 240 s duration, followed by 480 s of beam-off (dashed-orange line).

Fig. 11 Schematic drawing of the experiment time structure used for the individual configurations used during the experiment. See text for details

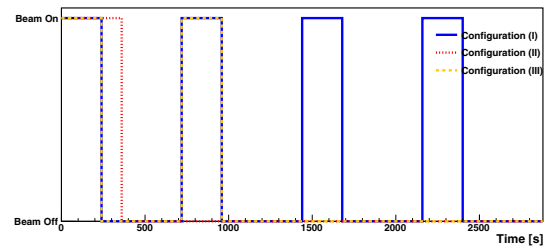
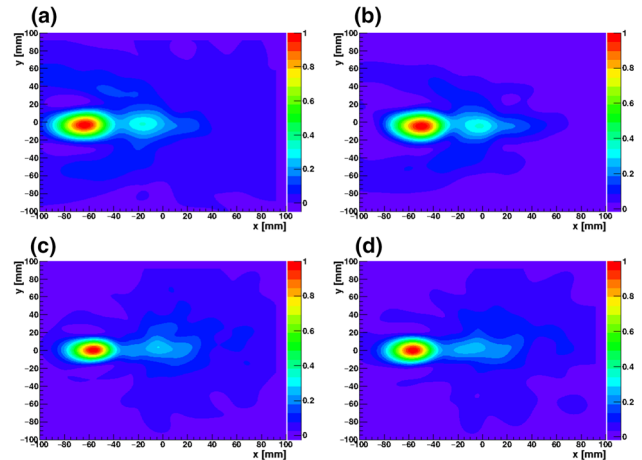


Fig. 12 Reconstructed experimental (panels **a** and **b**) and MC-calculated (panels **c** and **d**) Compton images from 4.4 MeV prompt γ -rays in configuration (I) for i-TED-A (panels **a** and **c**) and i-TED-B (panels **b** and **d**)



The following sections describe the PET- and Compton imaging results obtained for the three configurations just explained. For each configuration, the experimental results will be compared with the MC simulations. The three configurations are structured into beam-on (PG-Compton) and beam-off (PET) subsections.

5.1 Results for configuration (I)

5.1.1 Compton imaging in the beam-on lapses

The Compton images reconstructed from the experimental data acquired with i-TED-A and i-TED-B during the beam-on lapses of configuration (I) are displayed in panels (a) and (b) of Fig. 12. Panels (c) and (d) show the reconstructed MC images for i-TED-A and i-TED-B, respectively.

The reconstructed experimental and MC images for this configuration show a prominent maximum, which can be ascribed to prompt γ -rays emitted at the Bragg peak from the thick graphite layer. A secondary maximum can be inferred, particularly at the central region of the experimental image, corresponding to the geometric center of the setup where detection efficiency is largest. The fact that only the signature of the central Nylon layer can be appreciated indicates that detection sensitivity for prompt Compton imaging is not enough to resolve the other four thin Nylon layers, as expected from the MC-simulation. The ratio between the first and second maximum in the experimental and MC images changes from ~ 0.45 down to ~ 0.35 , respectively. This difference could be due to discrepancies between the evaluated cross-sections and/or stopping power in the libraries of the MC code and the actual cross-section values.

5.1.2 PET imaging in the beam-off lapses

The 2D PET image reconstructed from the experimental data of i-TED-A and i-TED-B during the beam-off intervals for configuration (I) is displayed in panel (a) of Fig. 13. The five irradiated layers are clearly observed and well resolved from each other. The maxima are well correlated with the position of the irradiated layers, as discussed below. The graphite layer is not visible in this image reconstruction because it was outside of the geometric PET field-of-view.

Figure 13b shows the x -axis projection of the 2D PET distribution together with a MC simulation of the β^+ emission of the activated layers. The weight of each individual layer contribution was chosen to match the height of the experimental distribution. While the experimental distributions for the first, second and last sample slots are relatively well reproduced by the MC simulations, the third and fourth distribution positions are slightly broader than those reconstructed from the MC calculations. A plausible explanation for this effect might be that the PLA matrix did not fit these two layers perfectly, and thus the mean free path of the β^+

Fig. 13 Panel **a** shows the experimental 2D PET image for Configuration (I). Panel **b** displays the x -projection (red) together with the MC simulations of the individual contributions (blue) and total (black)

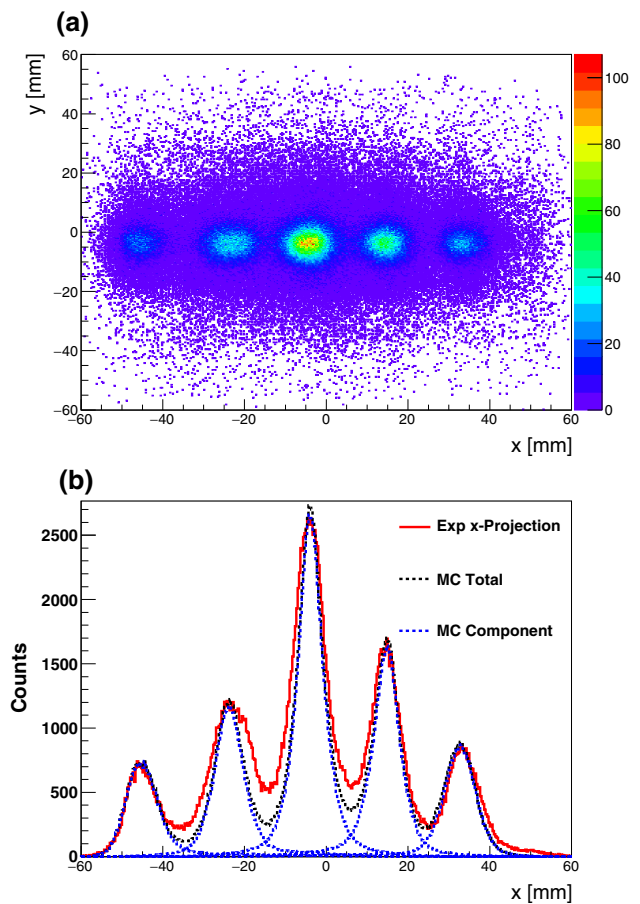


Table 3 The first column depicts the Nylon sample number for Configuration (I) starting from the beam direction

Nylon#	x [mm]	Δx [mm]	σ_{Exp} [mm]	σ_{MC} [mm]
1	33.46 (4)	-0.46(4)	4.16 (4)	4.22
2	14.33 (3)	0.67 (3)	4.41 (3)	4.03
3	-4.06 (2)	-0.06 (2)	4.22 (2)	3.94
4	-23.11 (3)	-0.89 (3)	5.53 (4)	4.17
5	-45.29 (6)	-0.71 (6)	4.07 (7)	3.99

The following columns show the values obtained for the mean value x reconstructed for each layer, its deviation with respect to the expected quantity (Δx), the width of each experimental distribution σ_{Exp} and the expected width σ_{MC}

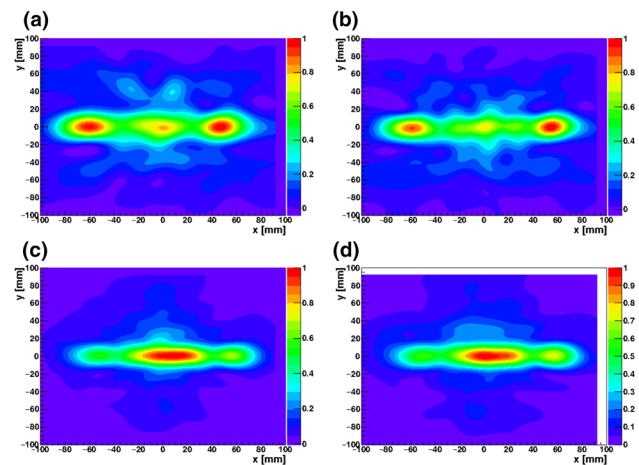
particles coming out from those irradiated layers was larger, thus leading to an additional broadening of the measured distributions at those locations.

The quality of the PET image can be quantified from the values listed in Table 3. The first column indicates the Nylon sample position. The second and third columns show the peak position from a Gaussian fit and shifts (Δx) with respect to the expected values given by the MC simulations. The width (σ) of the experimental distribution is listed in the 4th column, whereas the last column shows the widths (σ) from a Gaussian fit of the MC distribution.

There is a fair overall agreement between simulation and experiment. Sample positions are reconstructed via PET imaging always within a deviation of less than 1 mm. Variations in spatial resolutions are also, at most, of 1 mm with respect to expected MC values.

These results for Configuration (I) allow one to anticipate information on the complementarity between Compton and PET imaging. Whereas the beam-on Compton image for 4.4 MeV γ -rays is a relatively broad distribution (FWHM \sim 25 mm) but clearly correlated to the Bragg peak (Fig. 12), the beam-off PET technique offers a much finer resolution and sensitivity, although linked to the more indirect signature of the β^+ emitters.

Fig. 14 Reconstructed experimental (top panels **a** and **b**) and MC-calculated (bottom panels **c** and **d**) Compton images from 4.4 MeV prompt γ -rays in configuration (II) for i-TED-A (left) and i-TED-B (right)



5.2 Results for configuration (II)

5.2.1 Compton imaging in the beam-on lapses

Figure 14 shows the reconstructed Compton images for this configuration, both for the experimental data and the MC-simulation.

The most relevant aspect of the 2D distribution reconstructed for this configuration are the two prominent maxima in the experimental images, with comparable strengths, separated by about 120 mm. The first maximum at positive x -values corresponds to the location of the proton energy beam degrader. The second maximum on the left-hand side (negative x -values) coincides with the one found in configuration (I), which is therefore consistent with the position of the thick graphite layer or beam stopper. In addition, in the central region of the experimental Compton image one can appreciate another maximum, with a peak value that is only $\sim 20\%$ lower than the two main lateral peaks. Interestingly, for this configuration the reconstructed MC images do not reflect what is observed experimentally. The images for both i-TED modules show a maximum in the central part of the image, where the Compton detection efficiency is maximum. It is worth mentioning the $\sim 30\%$ difference in image intensity between the central part and the extremes, where the thick graphite stopper and proton–beam energy degrader are placed. This is nearly the same value, but in the opposite direction, when compared to the experimental images. At this moment we can only ascribe this notable discrepancy to possible deficiencies in the cross-sections present in the evaluated libraries used for the calculation, especially at low proton energies.

5.2.2 PET imaging in the beam-off lapses

Figure 15 shows the results obtained for the PET reconstruction of configuration (II). Interestingly, in addition to the five Nylon layers, the signature from β^+ annihilation events at the energy degrader is well observed at the right-hand side of the image ($x = 58$ mm), a position which is close to the edge of the PET field of view between both i-TED modules.

According to Fig. 15b and the values reported in Table 4 the positions reconstructed for the second and third layers are larger than those found in Configuration (I). The maximum deviation is 1.85 (4) mm, although the average deviation for PET-reconstructed positions is still of 1.0 (5) mm.

Apart from confirming the general conclusions obtained for Configuration (I), the measurement for Configuration (II) also shows that MC simulations for evaluating the Compton-imaging performance are less reliable than the corresponding calculations for PET imaging. This is to be ascribed, on the one side, to the better knowledge of the detector spatial response and overall performance for low-energy 511 keV γ -rays than for high-energy 4.4 MeV γ -rays and, on the other side, to the significant inaccuracies of ion-inelastic cross sections and γ -ray emission yields in the evaluated libraries used for MC studies, which may vary also significantly with ion-beam energy.

Fig. 15 Experimental 2D PET image for Configuration II (a). PET image x -projection (red) together with the MC simulations of the individual images (blue) and the total MC distribution (black) are shown in panel (b)

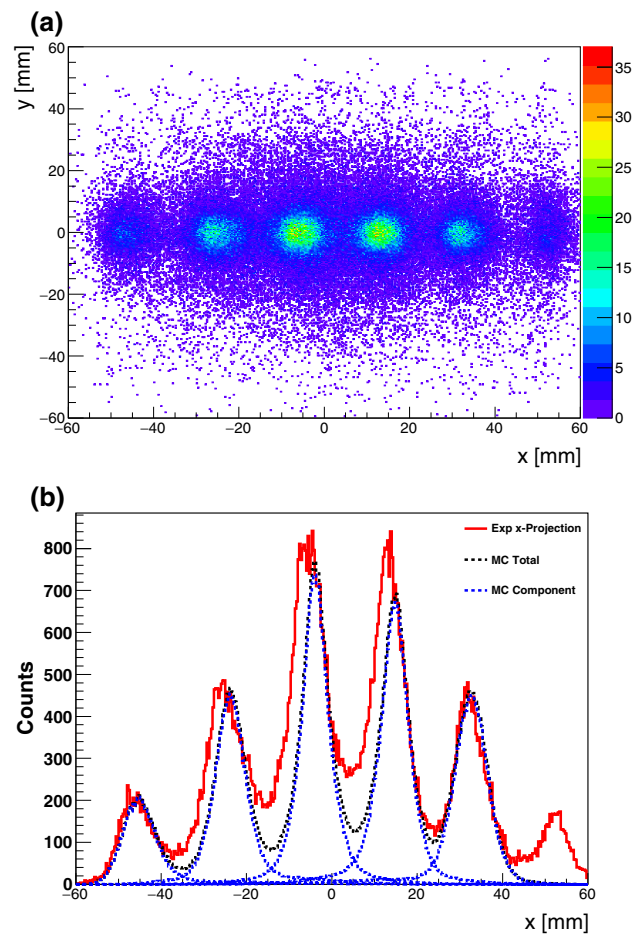


Table 4 The first column depicts the Nylon sample number for configuration (II) starting from the beam direction

Nylon #	x [mm]	Δx [mm]	σ_{Exp} [mm]	σ_{MC} [mm]
1	32.28 (5)	0.72 (5)	4.19 (5)	4.23
2	13.15 (4)	1.85 (4)	4.4 (4)	4.040
3	-5.35 (4)	1.35 (4)	4.57 (5)	3.95
4	-24.71 (5)	0.71 (5)	5.02 (6)	4.17
5	-46.5 (2)	0.5 (2)	4.1 (2)	4.0

The following columns show the values obtained for the mean value x of each layer, its deviation with respect to the expected quantity (Δx), its width σ_{Exp} and the expected width value σ_{MC}

5.3 Results for configuration (III)

5.3.1 Compton imaging in the beam-on lapses

The results shown in Fig. 16 for Configuration (III) are quite close to those found for Configuration (I) owing to similarities in the samples assembly, where essentially only the Nylon has been replaced by PMMA. These results help to assess the good repeatability of the Compton imaging technique and will not be discussed further.

5.3.2 PET imaging in the beam-off lapses

The results obtained for both i-TED detectors in PET mode for Configuration (III) are illustrated in Fig. 17 and quantified in Table 5. As for the previous configurations, the five layers can be clearly resolved and located quite reliably at the true positions, with an average deviation of only 1.1 (8) mm. This result confirms therefore the high accuracy and the good repeatability of the PET technique for this type of measurements.

Fig. 16 Reconstructed experimental (top) and MC-calculated (bottom) Compton images from 4.4 MeV prompt γ -rays in configuration (III) for i-TED-A (left) and i-TED-B (right)

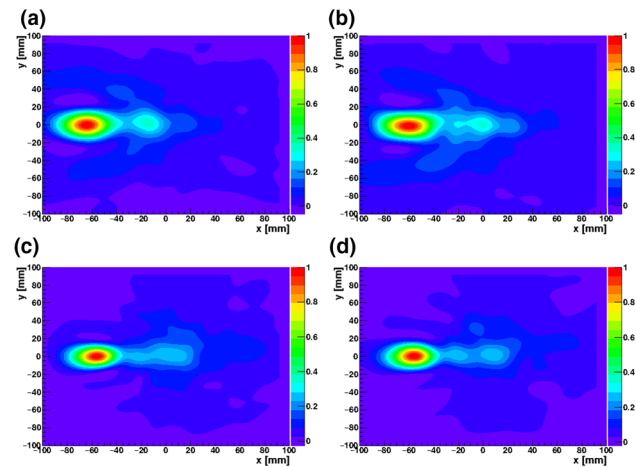
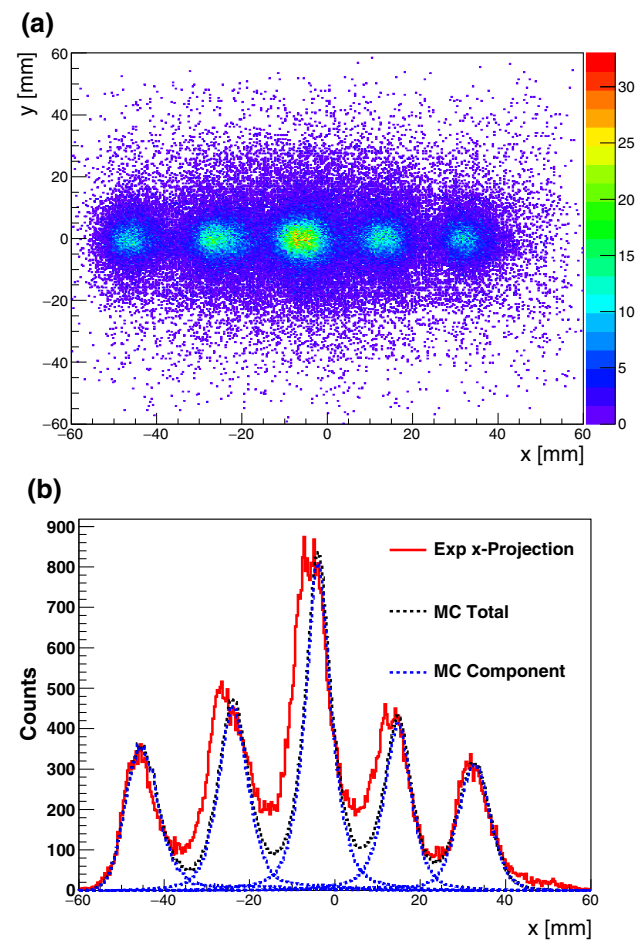


Fig. 17 Experimental 2D PET image for Configuration (III) is shown in panel (a). Panel b shows the 1D PET image x -projection (red) together with the Monte Carlo simulations of the individual images (blue) and the total (black)



The results obtained for Configuration (III) confirm the conclusions obtained for the previous two configurations and, in particular, allow one to assess the good repeatability of both Compton and PET techniques, given the agreement with the results found in Configuration (I). In this respect, it is worth to emphasize that Configuration (III) was measured on a different day than Configuration (I), after samples were exchanged from Nylon to PMMA and detectors were shut-down and brought up again. Finally, to a certain extent, the discrepancies of 1–2 mm found for the PET location of layers 2, 3 and 4 between Configuration (I) and (III) could be also ascribed to experimental inaccuracies of the sample holder assembly.

Table 5 The first column indicates the PMMA sample number starting from the beam direction

PMMA #	x [mm]	Δx [mm]	σ_{Exp} [mm]	σ_{MC} [mm]
1	32.34 (5)	0.66 (5)	4.09 (6)	4.22
2	12.82 (5)	2.18 (5)	4.76 (6)	4.03
3	-5.67 (3)	1.67 (5)	4.39 (4)	3.91
4	-24.93 (5)	0.94 (5)	5.20 (6)	4.15
5	-46.1 (1)	0.1 (1)	4.0 (1)	4.0

The following columns show the values obtained for the mean value x of each layer, its deviation with respect to the expected quantity (Δx), its width σ_{Exp} and the expected width σ_{MC}

Table 6 Maximum emission position for the thick graphite beam-stopper determined via Compton imaging for the three configurations and both i-TED modules

i-TED	Configuration		
	Max. Position in Compton (mm)		
	(I)	(II)	(III)
A	- 71.17	- 63.50	- 70.50
B	- 68.8	- 64.16	- 71.16
Δx	2.3	0.66	0.66

The bottom row shows the differences for each configuration between maxima of both imagers i-TED-A and i-TED-B

6 Discussion, conclusion and next steps

In this work we have demonstrated the possibility to use two modular Compton cameras in a front-to-front and synchronous configuration in conjunction with a pulsed proton beam to perform in situ prompt γ -ray Compton imaging and PET imaging, in a similar manner as conceptually proposed in Ref. [27]. This pilot experiment comprised a variety of materials and configurations, thereby aiming at evaluating both imaging techniques in terms of accuracy, sensitivity, repeatability and complementarity.

For the specific experimental conditions of the measurements reported herein with a low-energy proton beam, the γ -ray imaging performance of PET overcomes that of Compton imaging in terms of spatial resolution (6 mm vs. 24 mm) and detection sensitivity. The latter aspect is difficult to quantify in absolute terms, but visual inspection of the PET- and Compton-images clearly shows the capability of PET to visualize 0.8 mm thin plastic layers, whereas Compton-imaging is sensitive only to the bulk of γ -rays produced in the thick graphite layers, where a significant energy-loss of the proton-beam takes place. The very different performance in terms of sensitivity may not be the most relevant characteristic for ion-range monitoring, but it represents an aspect of potential interest when applying therapeutic beams to body regions where there can be a sudden change in tissue density due to air, bone, etc. As discussed in Sect. 1, this result for the higher spatial sensitivity of PET confirms its better suitability for monitoring physiological processes and tumour response during treatments with therapeutic beams.

The repeatability of the imaging technique may be more relevant for its application in ion-range monitoring, as discussed in Ref. [30]. The repeatability of our system for PET imaging can be evaluated from the Δx differences between measured maxima and reference MC values for the sample layers of the different configurations, as reported in Tables 3, 4 and 5. Maximum deviations of about 2 mm were found, with average deviations typically within ~ 1 mm. On the other hand, to estimate the repeatability in the reconstructed Compton images one can use the position of the maximum in each 2D-distribution measured with each i-TED imager for each configuration. These values are shown in Table 6. Deviations of up to 2.3 mm were found for Compton imaging, with an average value of 1.2 (9) mm for the three configurations. This result is comparable to the average variations measured for the samples with the PET technique.

It is worth to recall, however, that the Compton technique, despite its limitations in image resolution and detection sensitivity, shows the inherent advantage of being sensitive to the high-energy γ -rays that are both spatially and temporally directly correlated to the Bragg peak, thus providing more direct pristine information for ion-range monitoring.

Apart from the intrinsic systematic advantages and drawbacks of each imaging technique, an aspect which is of pivotal relevance for achieving real-time ion-range monitoring is the statistical significance attainable with each technique in a short period of time. In-room PET scanners have a much higher efficiency ($\varepsilon^{PET} \sim 2 \times 10^{-2}$) than prompt γ -ray imagers based on mechanical collimation ($\varepsilon^{Slit} \leq 10^{-3}$) [5] used for clinical studies [6]. However, for the combined system reported here based on i-TED modules, the efficiency for prompt γ -rays is much larger than that of a slit Camera, owing to the electronic collimation technique and the large

Table 7 Average count rates for Compton imaging in-spill and for PET imaging off-spill. Quoted quantities correspond to events in energy-selections utilized for PET and Compton imaging purposes in the three different configurations

	Configuration		
	Avg. Count Rate (Hz)		
	(I)	(II)	(III)
Compton in-spill	13324	6642	14975
PET off-spill	61	29	20

intrinsic and geometric efficiency of the position-sensitive detectors implemented [30]. For the exploratory measurements carried out in this work the average count rates in-spill and off-spill for each configuration and technique, Compton or PET, are reported in Table 7. Thus, on average, for the beam time-structure used in this work at CNA (see Fig. 11) a factor 300 higher counting rate was registered in-spill for Compton imaging, when compared to the statistics off-spill with the PET technique. Thus, under these particular test conditions, Compton imaging would become more suitable for real-time monitoring purposes than PET. However, this conclusion cannot be extrapolated to clinical conditions yet, where not only the beam duty cycle but also the cycle duration and the β^+ emitting isotopes contributing to the PET imaging need to be taken into account. Therefore, future test-measurements with clinical beam-energy conditions and with realistic treatment cycles will be therefore very convenient to explore and understand to which extent each one of the two independent imaging-techniques is contributing most to range verification, both from an statistical viewpoint aiming at real-time monitoring and from a systematic perspective aiming at enhanced accuracy. In summary, to a large extent both PET and PG Compton techniques may be rather complementary and they could be combined in a synergetic fashion to improve ion-range monitoring both in terms of statistical and systematic accuracy. Therefore, the possibility to combine them in a single and dedicated system, similar to the one reported here, seems a reasonable step forward that is worth exploring further in this field.

In future works we aim at overcoming the main limitations of the present study, which are related to the low proton-beam energy of 18 MeV, significantly smaller than common clinical values (100–200 MeV) and the long proton-irradiation cycles. The cyclotron at CNA was delivering a DC-beam and, for this reason, the beam on/off lapses had to be adjusted manually by the accelerator operator. They were also rather long, of about 100 s, in order to measure the corresponding beta-decay half-lives, which were the focus of another work [44]. Also, the low proton-beam energy led to the special target-phantom used, with several thin layers. Using a thick phantom with the available beam energy had not allowed for the detailed imaging study shown in this work. With a high beam energy big phantom volumes can be used. Therefore, next steps to develop further the hybrid Compton-PET technique comprise the realization of measurements using average clinical beam conditions and conventional water and PMMA phantoms. Using a pulsed beam of a high energy with a large phantom and a suitable duty cycle, it may become possible to correlate sequential PG-Compton and PET-images in- and off-spill, respectively, as it was proposed in Ref. [27]. In this respect, there are two main aspects to research in the future experiment. First, the performance of the detection system at the high counting rate conditions of the high-energy and high-intensity clinical beams needs to be validated. Second, one has to determine which is the optimal duty-cycle for the proton beam to accomplish both PG Compton and PET imaging aiming at a proper trade-off between statistical and systematic accuracy. If a pulsed-beam duty-cycle requirement of less than 0.01 is also confirmed at high beam-energy, this would align well with the application of this new hybrid methodology in treatments with superconducting synchrocyclotrons, which produce a pulsed beam (few μ s, every 1–2 ms) [51], and also with recent developments related to hybrid delivery approaches in flash therapy [52].

Acknowledgements T. Rodríguez-Gonzalez acknowledges the Spanish FPI predoctoral grant. M.C. Jiménez-Ramos acknowledges the support to this work through a VI PPIT-US contract. We would like to thank the crew at the Electronics Laboratory of IFIC, in particular Manuel Lopez Redondo and Jorge Náchar Arándiga for their excellent and efficient work. Finally, we would like to acknowledge the contribution of two anonymous referees, who provided valuable comments that helped us to improve the quality of this article.

Author Contributions JB-C contributed to investigation, methodology, formal analysis, data curation, visualization, and writing-original draft. JL-M contributed to investigation, methodology, formal analysis, and data curation. IL contributed to hardware, software, and visualization. CG contributed to conceptualization, methodology, supervision, investigation, and formal analysis. TR-G contributed to investigation, methodology, formal analysis, and data curation. MCJ-R contributed to conceptualization, methodology, supervision, investigation, and formal analysis. CD-P contributed to conceptualization, methodology, supervision, writing-review editing, funding acquisition, investigation, and formal analysis.

Funding Open Access funding provided thanks to the CRUE-CSIC agreement with Springer Nature. This work has been carried out in the framework of a project funded by the European Research Council (ERC) under the European Union's Horizon 2020 research and innovation programme (ERC Consolidator Grant project HYMNS, with grant agreement No.~681740). The authors acknowledge support from the Spanish Ministerio de Ciencia e Innovación under grants PID2019-104714GB-C21, FPA2017-83946-C2-1-P, FIS2015-71688-ERC, FPA2016-77689-C2-1-R, RTI2018-098117-B-C21, CSIC for funding PIE-201750I26 and from the European H2020-847552 (SANDA). This work was partially supported by Generalitat Valenciana PROMETEO/2019/007. J. Balibrea-Correa is supported by grant ICJ220-045122-I funded by MCIN/AEI/10.13039/501100011033 and by European Union NextGenerationEU/PRTR. J. Lereñdegui-Marco is supported by grant FJC2020-044688-I funded by MCIN/AEI/10.13039/501100011033 and by European Union-NextGenerationEU/PRTR.

Data Availability Statement This manuscript has associated data in a data repository. [Authors' comment: The datasets generated during and/or analysed during the current study are available from the corresponding author on reasonable request.]

Declarations

Conflict of interest The authors declare that they have no known competing financial interest or personal relationships that could have appeared to influence the work reported in this paper.

Open Access This article is licensed under a Creative Commons Attribution 4.0 International License, which permits use, sharing, adaptation, distribution and reproduction in any medium or format, as long as you give appropriate credit to the original author(s) and the source, provide a link to the Creative Commons licence, and indicate if changes were made. The images or other third party material in this article are included in the article's Creative Commons licence, unless indicated otherwise in a credit line to the material. If material is not included in the article's Creative Commons licence and your intended use is not permitted by statutory regulation or exceeds the permitted use, you will need to obtain permission directly from the copyright holder. To view a copy of this licence, visit <http://creativecommons.org/licenses/by/4.0/>.

References

1. A.-C. Knopf, A. Lomax, In vivo proton range verification: a review. *Phys. Med. Biol.* **58**(15), R131 (2013)
2. M. Durante, H. Paganetti, Nuclear physics in particle therapy: a review. *Rep. Prog. Phys.* **79**(9), 096702 (2016)
3. M. Durante et al., Charged-particle therapy in cancer: clinical uses and future perspectives. *Nat. Rev. Clin. Oncol.* **14**(8), 483–495 (2017)
4. M. Durante, Proton beam therapy in Europe: more centres need more research. *Br. J. Cancer* **120**(8), 777–778 (2019)
5. J. Krimmer et al., Prompt-gamma monitoring in hadrontherapy: a review. *Nucl. Instrum. Methods Phys. Res. Sect. A Accel. Spectrom. Detect. Assoc. Equip.* **878**, 58–73 (2018)
6. J. Smeets et al., Prompt gamma imaging with a slit camera for real-time range control in proton therapy. *Phys. Med. Biol.* **57**(11), 3371–3405 (2012)
7. I. Perali et al., Prompt gamma imaging of proton pencil beams at clinical dose rate. *Phys. Med. Biol.* **59**(19), 5849–5871 (2014)
8. J.C. Polf et al., Imaging of prompt gamma rays emitted during delivery of clinical proton beams with a Compton camera: feasibility studies for range verification. *Phys. Med. Biol.* **60**(18), 7085–7099 (2015)
9. E. Muñoz et al., Proton range verification with MACACO II Compton camera enhanced by a neural network for event selection. *Sci. Rep.* **11**, 9325 (2021)
10. P.G. Ortega et al., Noise evaluation of Compton camera imaging for proton therapy. *Phys. Med. Biol.* **60**(5), 1845–1863 (2015)
11. C.-H. Min et al., Prompt gamma measurements for locating the dose falloff region in the proton therapy. *Appl. Phys. Lett.* **89**(18), 183517 (2006)
12. E. Testa et al., Monitoring the Bragg peak location of 73 MeV/u carbon ions by means of prompt γ -ray measurements. *Appl. Phys. Lett.* **93**(9), 093506 (2008)
13. J.M. Verburg, J. Seco, Proton range verification through prompt gamma-ray spectroscopy. *Phys. Med. Biol.* **59**(23), 7089–7106 (2014)
14. W. Enghardt et al., Charged hadron tumour therapy monitoring by means of PET. *Nucl. Instrum. Methods Phys. Res. A* **525**(1–2), 284–288 (2004)
15. A. Miyatake et al., Measurement and verification of positron emitter nuclei generated at each treatment site by target nuclear fragment reactions in proton therapy. *Med. Phys.* **37**(8), 4445 (2010)
16. T. Nishio et al., The development and clinical use of a beam on-line PET system mounted on a rotating gantry port in proton therapy. *Int. J. Radiat. Oncol. Biol. Phys.* **76**(1), 277–286 (2010)
17. H.J.T. Buitenhuis et al., Beam-on imaging of short-lived positron emitters during proton therapy. *Phys. Med. Biol.* **62**(12), 4654–4672 (2017)
18. I. Ozoemelum et al., Real-Time PET imaging for range verification of helium radiotherapy. *Front. Phys.* **8**, 431 (2020)
19. I. Ozoemelum et al., Feasibility of quasi-prompt PET-based range verification in proton therapy. *Phys. Med. Biol.* **65**(24), 245013 (2020)
20. H. Tashima et al., A single-ring OpenPET enabling PET imaging during radiotherapy. *Phys. Med. Biol.* **57**(14), 4705–4718 (2012)
21. H. Tashima et al., Development of a small single-ring OpenPET prototype with a novel transformable architecture. *Phys. Med. Biol.* **61**(4), 1795–1809 (2016)
22. H. Tashima et al., 3D Compton image reconstruction method for whole gamma imaging. *Phys. Med. Biol.* **65**(22), 225038 (2020)
23. E. Yoshida et al., Whole gamma imaging: a new concept of PET combined with Compton imaging. *Phys. Med. Biol.* **65**(12), 125013 (2020)
24. P. Dendooven et al., Short-lived positron emitters in beam-on PET imaging during proton therapy. *Phys. Med. Biol.* **60**(23), 8923–8947 (2015)
25. J. Bauer et al., An experimental approach to improve the Monte Carlo modelling of offline PET/CT-imaging of positron emitters induced by scanned proton beams. *Phys. Med. Biol.* **58**(15), 5193 (2013)
26. C. Kurz et al., Investigating the limits of PET/CT imaging at very low true count rates and high random fractions in ion-beam therapy monitoring. *Med. Phys.* **42**(7), 3979–3991 (2015)
27. K. Parodi, On- and off-line monitoring of ion beam treatment. *Nucl. Instrum. Methods Phys. Res. A* **809**, 113–119 (2016)
28. C. Lang et al., Sub-millimeter nuclear medical imaging with high sensitivity in positron emission tomography using $\beta^+\gamma$ coincidences. *J. Instrum.* **9**(1), P01008 (2014)
29. C. Domingo-Pardo, i-TED: a novel concept for high-sensitivity (n,γ) cross-section measurements. *Nucl. Instrum. Methods Phys. Res., Sect. A* **825**, 78–86 (2016)
30. J. Lerendegui-Marco et al., Towards machine learning aided real-time range imaging in proton therapy. *Sci. Rep.* **12**, 2735 (2022)
31. J. Lerendegui-Marco et al., Simultaneous neutron and gamma imaging system for real time range and dose monitoring in hadron therapy and nuclear security applications. *EPJ Web Conf.* **261**, 05001 (2022)
32. Javier Balibrea-Correa et al., First in-beam tests on simultaneous PET and Compton imaging aimed at quasi-real-time range verification in hadron therapy. *EPJ Web Conf.* **261**, 05002 (2022)
33. J. Gómez-Camacho et al., Research facilities and highlights at the Centro Nacional de Aceleradores (CNA). *Eur. Phys. J. Plus* **136**(3), (2021). <https://doi.org/10.1140/epjp/s13360-021-01253-x>
34. A. Baratto-Roldán et al., Preparation of a radiobiology beam line at the 18 MeV proton cyclotron facility at CNA. *Phys. Med.* **74**, 19–29 (2020)

35. V. Babiano et al., First i-TED demonstrator: a Compton imager with dynamic electronic collimation. *Nucl. Instrum. Methods Phys. Res., Sect. A* **953**, 163228 (2020)
36. J. Balibrea-Correa et al., Machine learning aided 3d-position reconstruction in large LaCl_3 crystals. *Nucl. Instrum. Methods Phys. Res. Sect. A* **1001**, 165249 (2021)
37. ERC European project. ERC-Consolidator Grant Agreement No. 681740, HYMNS, High-sensitivity Measurements of key stellar Nucleo-Synthesis reactions (2016-2022), PI: C. Domingo Pardo. <https://cordis.europa.eu/project/id/681740>. Accessed Oct 2022
38. V. Babiano-Suárez et al., Imaging neutron capture cross sections: i-TED proof-of-concept and future prospects based on Machine-Learning techniques. *Eur. Phys. J. A* **57**(6), 197 (2021)
39. A. Di Francesco et al., TOFPET 2: high-performance circuit for PET time-of-flight. *Nucl. Instrum. Methods Phys. Res. Sect. A Accel. Spectro. Detect. Assoc. Equip.* **824**, 194–195 (2016)
40. D. Schug et al., Crystal delay and time walk correction methods for coincidence resolving time improvements of a digital-silicon-photomultiplier-based PET/MRI insert. *IEEE Trans. Radiat. Plasma Med. Sci.* **1**(2), 178–190 (2017)
41. P. Olleros et al., On the performance of large monolithic $\text{LaCl}_3(\text{Ce})$ crystals coupled to pixelated silicon photosensors. *J. Instrum.* **13**(03), P03014–P03014 (2018)
42. A. Baratto-Roldán et al., Feasibility study of a proton irradiation facility for radiobiological measurements at an 18 MeV cyclotron. *Instruments* **2**(4), 26 (2018)
43. T. Rodríguez-González et al., Production yields of emitters for range verification in proton therapy. *EPJ Web Conf.* **239**, 24003 (2020)
44. T. Rodríguez-González et al., Production yields at the distal fall-off of the + emitters ^{11}C and ^{13}N for in-vivo range verification in proton therapy. *Radiat. Phys. Chem.* **190**, 109759 (2022)
45. T. Tomitani, M. Hirasawa, Image reconstruction from limited angle Compton camera data. *Phys. Med. Biol.* **47**(12), 2129–2145 (2002)
46. O. Klein, Y. Nishina, Über die Streuung von Strahlung durch freie Elektronen nach der neuen relativistischen Quantendynamik von Dirac. *Z. Phys.* **52**(11), 853–868 (1929)
47. J. Nickolls et al., Scalable parallel programming with CUDA. *Queue* **6**(2), 40–53 (2008)
48. J. Allison et al., Recent developments in Geant4. *Nucl. Instrum. Methods Phys. Res. Sect. A* **835**, 186–225 (2016)
49. J.M. Verburg et al., Simulation of prompt gamma-ray emission during proton radiotherapy. *Phys. Med. Biol.* **57**(17), 5459–5472 (2012)
50. K. Parodi, J.C. Polf, In vivo range verification in particle therapy. *Med. Phys.* **45**(11), e1036–e1050 (2018)
51. J. Yap et al., Future developments in charged particle therapy: improving beam delivery for efficiency and efficacy. *Front. Oncol.* **11**, 780025 (2021)
52. S. Jolly et al., Technical challenges for flash proton therapy. *Phys. Med.* **78**, 71–82 (2020)